7-2-2012

Isothermal helium flow measurements twrough a rectangular channel for a Wide Knudsen range

John Anderson

John M. Anderson
Candidate

Mechanical Engineering
Department

This thesis is approved, and it is acceptable in quality and form for publication:

Approved by the Thesis Committee:

Dr. Tariq Khraishi , Chairperson

Dr. Ron Manginell

Dr. Yu-Lin Shen

ISOTHERMAL HELIUM FLOW MEASUREMENTS THROUGH A RECTANGULAR CHANNEL FOR A WIDE KNUDSEN RANGE

by

JOHN M. ANDERSON

B.S. MECHANICAL ENGINEERING
UNIVERSITY OF NEW MEXICO, 2005

THESIS

Submitted in Partial Fulfillment of the
Requirements for the Degree of

Master of Science
Mechanical Engineering

The University of New Mexico
Albuquerque, New Mexico

May, 2012

Acknowledgments

I would like to express my deepest appreciation to Dr. Ron Manginell for his many years of mentorship. His guidance and support have been most important to my success as a student and as a mechanical engineer. The countless hours of insight provided by Dr. Manginell have been invaluable to this journey.

I would like to thank my colleague and friend Matt Moorman for his suggestions and encouragement as well as Dr. John Torczynski for clarifying any theory-based confusion that occurred more than once.

Finally, I would like to thank my advisor, Dr. Tariq Khraishi, for his support and encouragement throughout this endeavor as well as Dr. Yu-Lin Shen for his participation on my thesis committee.

Experiments and data evaluation for this thesis were performed at Sandia National Laboratories in Albuquerque, NM.

Sandia National Laboratories is a multi-program laboratory managed and operated by Sandia Corporation, a wholly owned subsidiary of Lockheed Martin Corporation, for the U.S. Department of Energy's National Nuclear Security Administration under contract DE-AC04-94AL85000.

Isothermal Helium Flow Measurements Through a Rectangular Channel for a Wide Knudsen Range

by

John M. Anderson

B. S., Mechanical Engineering, University of New Mexico, 2005

M. S., Mechanical Engineering, University of New Mexico, 2012

Abstract

The purpose of this experimental investigation is to measure the isothermal steady flow of Helium through a rectangular microchannel from the continuum to the free-molecular regime. The intention is to expand the measured Knudsen number range for rectangular cross section microchannels as compared with that presently found in literature. As presented, the Knudsen range for the experiments is 0.03 to over 500. A dual tank accumulation technique was chosen for flow measurements which allows for very low flow rate measurements ($< 10^{-13}\mathrm{kgs}^{-1}$). Experimental results were evaluated against analytical solutions for the continuum, slip, and free molecular regimes as well as a closed-form equation that would include any regime. Data was also compared to computer models using the Direct Simulation Monte Carlo method.

Table of Contents

List of Figures

Chapter 1

Introduction

The dimensionless Knudsen number (Kn) is a key parameter in determining the behavior of a gas and is defined as the ratio of the mean free path to the characteristic physical length, referring to the distance between surfaces having the most influence on the molecules in a particular flow geometry. As a gas is rarefied, the molecules' average mean free path increases. The mean free path is defined as the average distance traveled between two similar events, such as elastic collisions of molecules in a gas. Rarefying a gas is one way to increase Kn. Another way to increase Kn is to decrease the characteristic physical length; for example, decreasing the diameter of a cylindrical tube, or in our case, decreasing the channel height. At high Kn ($\mathrm{Kn} > 10$), the molecules collide much more with the surfaces that the representative physical length separates, than with each other. As a result one must take into account the quality of the surface when calculating flows in this regime. In gas flows with small Kn ($\mathrm{Kn} < 0.1$), viscosity effects dominate due to intermolecular collissions occurring much more often than with the surrounding surface. A large Kn may result either from small physical features or from a low pressure environment.

High Knudsen number flows arise frequently in engineering applications from upper atmosphere aerodynamics to micro-electromechanical system (MEMS) devices. For many sensors and MEMS, operation under vacuum has become a key factor to increasing performance. RF MEMS switches and Micro Mass Spectrometers, for example, see improved performance at reduced pressure. Simply put, the need to further

understand rarefied gas flow occurring in and around a variety of dimensions and geometries has prompted many experimental flow studies.

Many papers on gas micro flows have been published over the past few decades in pursuit of fully understanding rarefied gas-surface interactions in micro-dimensions. Gas flow through microtubes of various dimensions has been measured from the continuum to the free-molecular regime (Porodnov, Suetin et al. 1974; Ewart, Perrier et al. 2007; Marino 2009). Flow through microchannels has also been explored, but the channel dimensions and driving pressures resulted in a regime where the Knudsen number stayed in the low double digit range (Sharipov 1999; Ewart, Perrier et al. 2007). Some experiments were through a single tube or channel while others measured flow through several corridors in parallel. As recently as 2011 flow through an array of sub-10-nm pores resulted in a Knudsen number of approximately 10 at atmospheric conditions (Fissell, Conlisk et al. 2011). The intention here is to provide a data set in contribution to further understanding rarefied gas dynamics.

Experimental techniques have progressed as an effect of this pursuit. In the late 1990s, a dual-tank accumulation technique for measuring very small flows was developed and proved to be very accurate (Arkilic, Schmidt et al. 1997). This method consists of two constant volume tanks on each side of the path of interest (channel or microtube), thus called the 'constant volume' technique. The tanks are large compared to the path of interest, so the flow is constant for the duration of each experiment. This method proved to be an accurate method for measuring very small flows down to 10^{-13} kg/s^{-1} and possibly lower depending on equipment capabilities.

In experiments by Arkilic, the inlet and outlet pressures were near atmospheric so

the Knudsen number only ranged from 0.03 to 0.45 through a 1.33 μm tall channel, never transitioning out of the continuum regime. Ewart (2006) conducted experiments in which flow through microtubes of 18.2 mm in length with an inner diameter of 49.6 μm was measured. For the tube experiments, the Knudsen number ranged from 0.003 to 30. As with Arkilic's experiments, theoretical calculations were compared to experimental data. Flow measurements have not been limited to single gases, for example; argon and helium have been combined at different ratios to form binary gases for flow experiments (Szalmas, Pitakarnnop et al. 2010). Pitakarnnop (2009) integrated two flow measuring techniques, the 'constant volume' method and the droplet tracking method in the same experimental rig for "double-checking" flow rates. His experiments measured flows as low as $3x10^{-12}$ kg s^{-1} at a Knudsen number of 1.4 across 45 parallel microchannels of 1.88 μm height (Pitakarnnop, Varoutis et al. 2009).

In experiments published by Ewart (2007), a rectangular channel, 9.39 mm in length, 492 μm in width, and 9.38 μm in height, was used. In this work, the outlet pressure was maintained at 0.2 times the inlet pressure, and his lowest measurement was with an outlet pressure of 12 Pa. The Knudsen numbers for this set of experiments ranged from 0.03 to 50 (Ewart, Perrier et al. 2007). According to Ewart, experimental equipment such as the vacuum pump and pressure sensor limitations restricted the Knudsen number and prevented flow from reaching far into the free molecular regime. The lowest mass flow measured by Ewart in 2007 was 10^{-13} kgs^{-1} with the experimental error estimated to be +/-4.5%.

To date, the channel dimensions and equipment used in published experiments has restricted Kn to 50 in a rectangular channel. As previously mentioned, the Kn may be

increased by decreasing device size or reducing pressure. Here we present flow measurements through different microchannel dimensions of 9.67μm and 4.5 μm in height. The resulting Knudsen number in the 4.5μm channel is approximately two times higher than that of the 9.67μm at the same driving pressures. At an outlet pressure of 12 Pa with $P_{in}/P_{out} = 5$ the mean Knudsen number in the channel is approximately 50 in a channel with a 10 μm height and 110 in a channel with a 4.5 μm height. However, this is not the first time channel height has been decreased to increase the Knudsen number. Fissel (2011) measured flow at high Knudsen numbers by decreasing the effective dimension of channels, but kept pressures near atmospheric conditions limiting the Knudsen number to 10 (Fissell, Conlisk et al. 2011).

Advances in fabrication methods allow for accurate controllability of channel dimensions, and the use of plasma-assisted bonding assures that the physical/chemical properties of the channel walls are similar (polished silicon), reducing modeling/simulation complexity. The use of primary standard pressure gauges in our vacuum apparatus allowed flow measurements as low as 10^{-13} kgs^{-1}. Our experimental data is evaluated against that published by Ewart in Fig. 10; it was then evaluated against analytical equations based on computer models for the continuum, slip, and free molecular regimes. In the FMF regime, tedious simulations using the Direct Simulation Monte Carlo (DSMC) method provided the most accurate and easy to use flow model across all of the flow regimes (Gallis and Torczynski 2012). The goal of this thesis is to provide a data set to compare to models that may be used in future MEMS design.

2. Channel Design and Fabrication

2.1 Channel Design

There are several characteristics of the channel that may affect flow, from dimensions, to channel wall roughness and composition. The ratios of the channel's width (W), height (H), and length (L) are important parameters to consider when designing a channel. If dimensions are chosen correctly, flow modeling can be simplified. First, if $L \gg W$, the channel end effects may be ignored. Secondly, if $W \gg H$, the lateral wall effects may be neglected. The result of these simplifications is a long channel with a very shallow height compared to its width that is more easily modeled, as end effects and wall effects can be minimized for most Kn values. Actual dimensions are described in section 2.2. Flow modeling is also simplified if the composition and roughness of the floor and ceiling of the flow channel are similar. To accomplish this, polished silicon was used for both surfaces in this thesis, an improvement upon prior research. This required the use of direct bonding, which is also described in 2.2.

2.2 Channel Fabrication

A combination of two channel lengths and two channel heights are used for the experiments making a total of four different channel dimensions tested. The two different lengths are 1cm and 0.5cm and the two different channel heights are 4.5 μm and 9.67 μm, all with a channel width of 500 μm. Plenum volume is greater than 100 times the channel volume to ensure that the flow channel is responsible for the measured flow characteristics. A computer-generated schematic of the channel is depicted in Fig. 1

below.

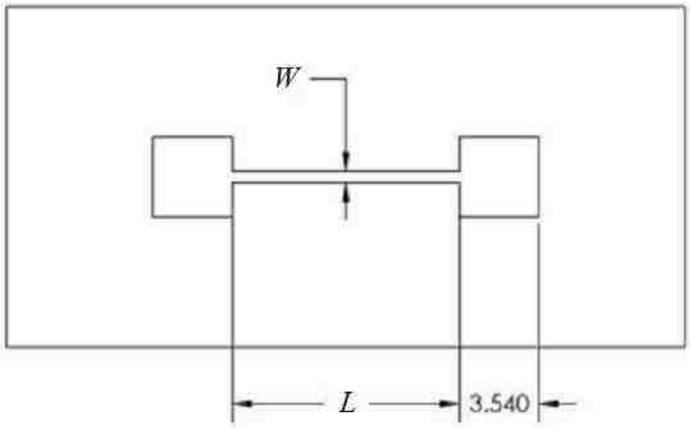

Figure 1 Schematic of test channel with inlet and outlet plena. *W* is the channel width, *L* is the channel length, and *H* (not shown) is the channel height normal to the viewing plane. Dimensions shown are in mm.

In order to use single crystal silicon for the channel floor and ceiling, a silicon-silicon direct bonding technique is an excellent choice. Direct bonding is a proven method to assure a hermetic seal required for accurate, reliable data. Several articles have been written on the direct bonding process and the benefits of the mild bonding conditions to microelectronics (Schmidt 1994; Howlader 2010). Obviously, cleanliness of the substrates to be bonded is critical for a hermetic seal, as stressed in literature (Farrens, Dekker et al. 1995).

Silicon on insulator (SOI) wafers were chosen as the starting material to provide an accurate method to control channel height. The device layer thickness plus the buried oxide (BOx) thickness determine the channel height. The 4.5 μm channel is the result of the 3.5 μm device layer plus the 1 μm BOx layer. A 8.67 μm device layer is used to

construct the 9.67 μm channel in a similar fashion. Unfortunately, the buried oxide exerts approximately 270 MPa compressive stress on the handle substrate. The stress causes enough wafer bow to hinder the direct bonding process. Deviations from a perfectly flat wafer, including imperfections and particulates, greatly reduce bond strength and quality in the direct bonding process (Lin, Ma et al. 2006; Tang, Peng et al. 2009). To counteract the wafer bow, a 1μm thermal oxide was grown and then removed only from the device side of the wafer. All wafer bow measurements are listed in Appendix E.

Another imperfection presents itself as a result of the SOI manufacturing process. A small 0.25 μm lip can be measured around the edge of the device side of the wafer which was sufficient to impede bonding. This lip can be removed using an edge bead removal lithography process and dry etch. Once the wafer is flat and free of micro-protrusions, the process flow may proceed. Standard photolithography is used to transfer the patterns to the device and handle sides of the wafer. An Alcatel AMS-100 deep reactive-ion etcher (DRIE) is used to etch the all patterned features, resulting in relatively smooth, vertical sidewalls shown in Fig. 2. The now-exposed buried oxide on the channel floors is then wet etched in buffered oxide etch diluted 6:1 with deionized (DI) water. The wet oxide etch causes some undercut apparent in Fig. 2, but the small notch has negligible effects because the channel width is much greater (500 μm) than the channel heights (9.67 μm and 4.5 μm).

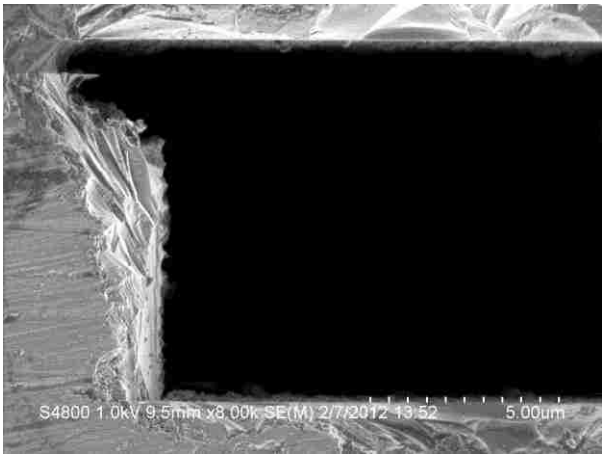

Figure 2 The vertical sidewall profile of 10-micron channel via SEM. The notch at the top corner is due to undercut of the buried oxide in the wet oxide etch step.

All organics from the photoresist and the DRIE process must be removed before proceeding. A new single crystal wafer will be bonded to the etched wafer to form a closed channel using a direct bonding technique. The substrates must be dipped in dilute hydrofluoric acid (100:1) for sixty seconds to remove any native oxide. The substrates are then rinsed in DI water before entering a Standard Clean number 1 (SC1) bath, which also assists in activating the silicon surface for bonding. The SC1 consists of a 60:4:1 H_2O:H_2O_2:NH_4OH solution heated to 40 ºC for 10 minutes with 50 Watts of mega sonic agitation. The activation is completed by exposing the substrate surfaces to an O_2 plasma in Plasmatherm reactive ion etcher (RIE) (25 W, 300 seconds). The activation creates a large number of free silanol [Si-OH] chemical bonds . The two wafers are then simply brought together and pressure is applied by hand from the center of the wafer outward. The silanol bonds from each surface react to form siloxane [Si-O-Si] bonds shown in Fig. 3, releasing water and hydrogen in the process (Howlader, Suehara et al. 2006).

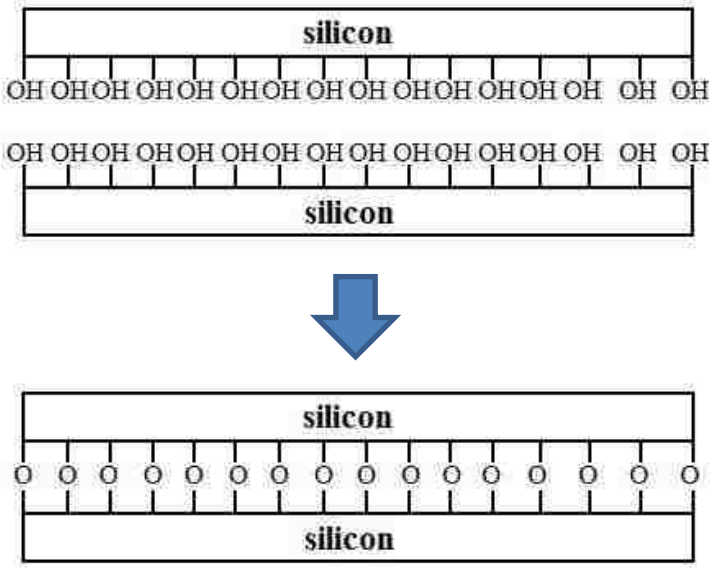

Figure 3 The chemical reaction that occurs during the direct bonding process releases H_2 and H_2O.

The bonded wafers are then annealed at 200 ºC for 2 hours to strengthen the bond and then inspected using C-mode scanning acoustic microscopy (CSAM).

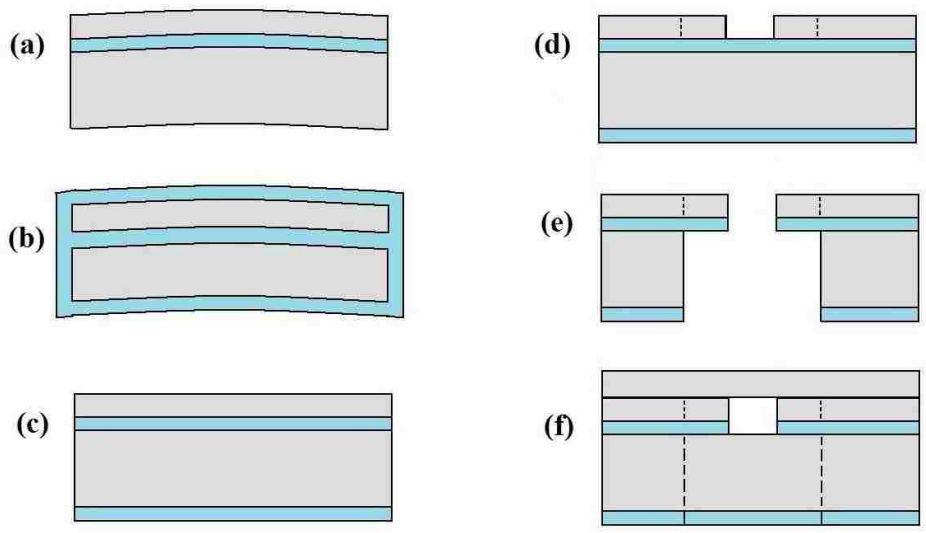

Figure 4 This cross-sectional schematic sequentially depicts the channel fabrication steps. The light blue represents silicon dioxide and the light gray represents silicon. The figures are not to scale. The wafer bow is exaggerated in (a) and (b) as are the relative dimensions. (b) Illustrates growth of the bow-compensating oxide, while (c) shows removal of the oxide from top surface to compensate bow. Step (d) shows the channel formed by DRIE and (e) shows the plenum at one end of the channel. Step (f) depicts the bonded channel lid at mid-channel, while the plena are indicated by the dashed lines.

Wafer-level C-mode scanning acoustic microscopy (CSAM) is used to verify bond quality, acknowledge voids or unbonded areas, and to check individual channels for potential leak paths (CSAM has 20 micron pixel resolution). With the use of CSAM imaging shown in Fig. 5, channels could be qualified for flow experiments.

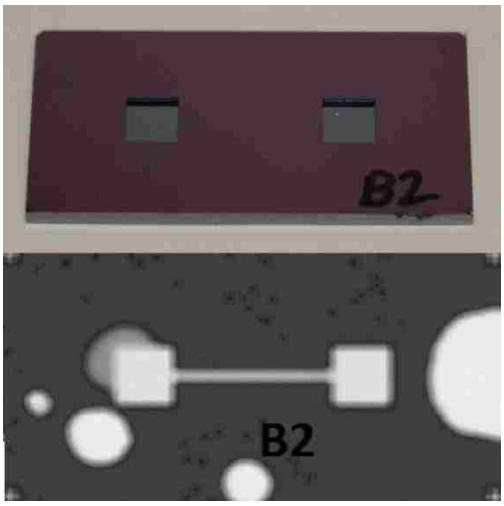

Figure 5 Top: Photograph of fabricated channel chip. Bottom: Image of same channel in top photo generated by C-mode scanning acoustic microscopy (CSAM). The imaging method shows a contrast between bonded areas (dark areas) and voids (light areas) so only quality channels are chosen for testing.

Once diced, only channels proven to be completely bonded by CSAM are chosen for fitting assembly and leak testing. To connect the channels to the vacuum flow apparatus, fused silica capillaries and capillary fittings are required. Channels are bonded to capillary fittings (Upchurch Nanoport Fitting, Part N-333) with the epoxy ring provided with the fitting kit, circled in Fig. 6. The capillary chosen for the experiments is composed of fused-silica with 660 μm o.d. with a 530 μm i.d. from Polymicro Technologies©.

Figure 6 A Nanoport fitting is plumbed to quadrupole mass spectrometer for He leak test.

The assembled fittings must pass the helium leak test to assure flow measurements are isolated from any external effects. To leak test the fitting and channel assembly, one end of the channel is plumbed to a quadrupole mass spectrometric detector. The mass spectrometer is specifically tuned for helium. The other end is left open while the system is pumped to verify flow through the channel. The open end is then capped and the channel is pumped down to 10^{-4} Torr (0.1333 Pa). Helium is released around the outside of the system. If a leak exists anywhere between the silicon-silicon bond or in the fittings, helium will be sucked in and detected by the mass spectrometric detector. Once hermiticity is verified by the absence of helium signal, the assembly is ready for flow testing. The channel/fitting assembly is leak tested for leak rates of 10^{-9} (atm)ccs^{-1} (1.786 x 10^{-15} kgs^{-1}), which is about 1% of our lowest flow measurement.

3 Experimental Methods

3.1 System

The microchannel is plumbed in series between two constant volume tanks (see Fig. 7). The inlet and outlet tanks are considered to be very large compared to the volume of the channel. This guarantees that the microflow parameters are independent of time during the course of a typical experiment. The system is contained in a controlled environment, so isothermal flow is assumed. Temperature variations will be measured and considered in the experimental error calculation. The turbo pump is used for any measurements requiring tank pressure below 200 Pa. Knudsen numbers can easily reach into the hundreds with the employed pumps in the channel dimensions used.

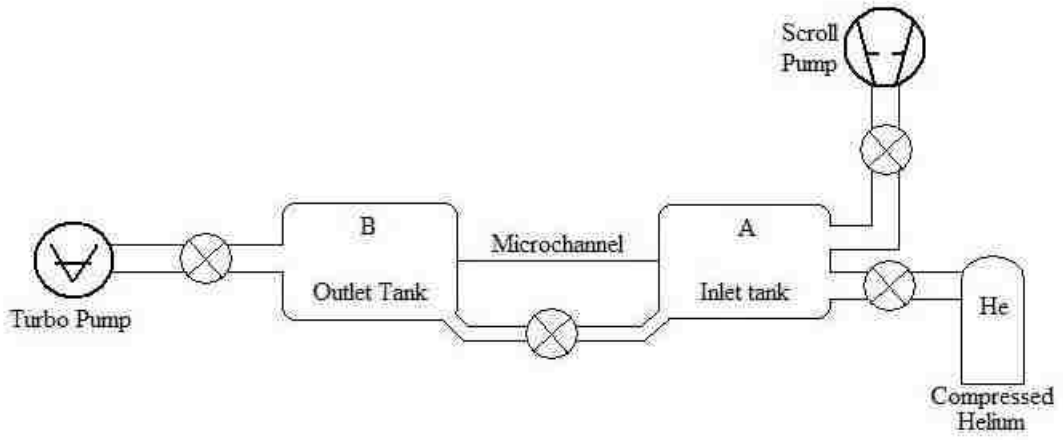

Figure 7 Schematic of the vacuum system used for the constant volume measurement method.

3.2 Flow Measurements

The ‘constant volume’ method used to measure flow through the channel consists of measuring a small pressure change in either the inlet tank or the outlet tank. For this set

of experiments, the increase in outlet pressure was used to calculate flow. From the ideal gas law, the change in mass, dm, over the duration of the experiment, τ, can be calculated.

$$P_{out}V_{out} = m\boldsymbol{R}T, \tag{1}$$

where V_{out} is the volume of the outlet tank. This value is measured to be 412.5 cc (+/- 8 cc) using a calibrated volume tank and the $P_1V_1 = P_2V_2$ method and remains constant throughout all of the experiments. The value $\boldsymbol{R}$ is the specific gas constant for helium. The value P_{out} is recorded at 10 Hz for the duration of each experiment, as is the temperature T. A relationship between the varying terms in Eq. 1 may be written as:

$$\frac{dP_{out}}{P_{out}} = \frac{dm}{m} + \frac{dT}{T} \tag{2}$$

During the time τ for the outlet tank to increase in pressure by 1%, the inlet tank is expected to decrease by 0.2% since the inlet tank has five times the pressure of the outlet tank. Dividing the two terms of (2) by the experimental time τ the following equation may be obtained:

$$\frac{dm}{\tau} = \frac{V}{RT}\frac{dP_{out}}{\tau}\left(1 - \frac{dT/T}{dP_{out}/P_{out}}\right) \tag{3}$$

Due to the fact that the observed temperature variation was less than half a degree, the last term in (3) is much smaller than unity and can be ignored. Thus, the change in mass in the outlet tank over time:

$$\frac{dm}{\tau} = \frac{V}{\boldsymbol{R}T}\frac{\delta P_{out}}{\tau} \tag{4}$$

is the isothermal mass flow rate through the micro channel. To determine the mass flow

rate for each experiment, the recorded pressure readings are plotted versus the time, τ, that is required for the outlet reservoir pressure to increase by 1%. The last term in (4) may be calculated from the linear fitting function,

$$P(t) = at + b, \qquad a = \frac{\delta P_{out}}{\tau} \ , \tag{5}$$

Where *a* is simply the slope line when the pressure is plotted against time as shown in Fig. 8 for a typical flow measurement. The measurement in Fig. 8 provides a single data point for one of the plots in Fig. 9.

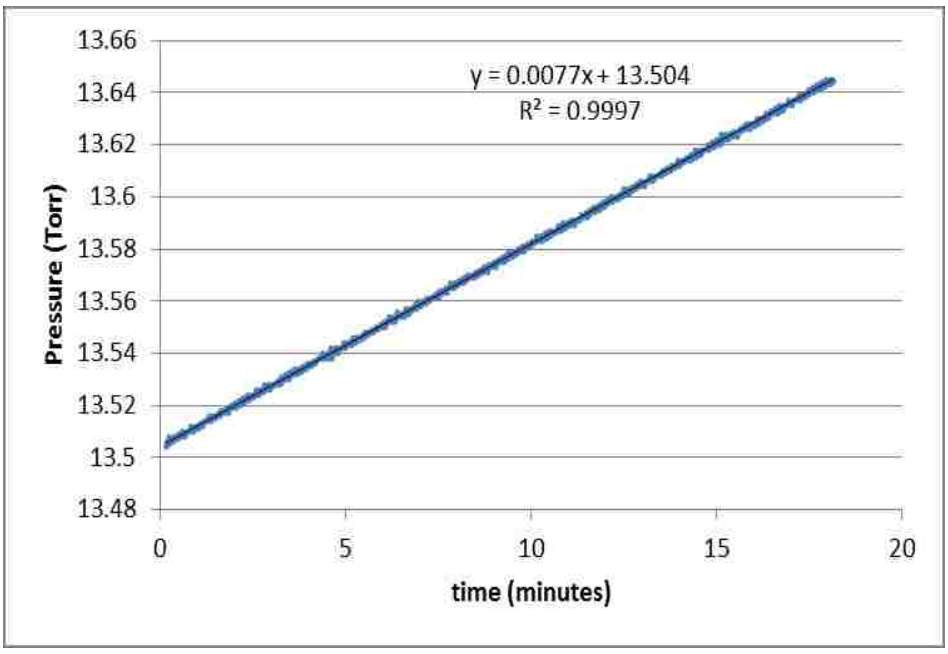

Figure 8 The raw data plotted against time showing an a-value of 0.0077 and an R^2 value of 0.9997.

In order for the data to be credible at such small pressure changes, the experimental error must be calculated. Temperature measurement during the course of

the experiments confirmed that flow was essentially isothermal with an observed variation of less than 0.5 K. The pressure transducer used for setting the outlet and inlet pressures for each measurement is Paroscientific model 745-15A. Once the inlet and outlet reservoirs are isolated, the Paroscientific 745-15A is used for the outlet tank and a Paroscientific model 6000-45A-226 is used to monitor the inlet pressure. The pressure sensors are rated at 0.01% accuracy on the inlet and better than 0.008% accuracy on the outlet side. These variations are smaller than the expected experimental error and are consistent with steady flow assumptions. The evaluation of the measurement errors from (4) and (5) are as:

$$\frac{\Delta Q_m}{Q_m} = \frac{\Delta V}{V} + \frac{\Delta T}{T} + \frac{\Delta a}{a} \tag{6}$$

where $\Delta T/T$, accounts for the non-isothermal effects evaluated at ±2% (Graur, Méolans et al. 2005). $\Delta V/V$ is the uncertainty of the volume measurement, ±2%. $\Delta a/a$ is the error on the coefficient a in (5) and is evaluated at ±0.5% at the higher pressures, but increases to ±1% at the lower pressures. Combining these gives us a maximum percent error of ±5% at any time.

4 Results and Discussion

In rarefied gas dynamics, as the mean free path length increases, molecules start to interact with structure surfaces more than each other. Depending on the pressure and the dimensions of the prevailing surface, the gas may behave as continuous, free-molecular, or transitioning from one to the other. As described in the introduction, the dimensionless

Knudsen number (Kn) is the ratio of the mean free path length to the characteristic dimension, i.e. tube diameter or channel height. The continuum regime describes the behavior of the gas when $0 < Kn < 0.001$. As Kn increases to the range of $0.001 < Kn < 0.1$, the gas is considered to be in the slip regime and molecules start to spread and interact more with the surface and less with each other. From $0.1 < Kn < 10$, the behavior of the gas is transitioning from slip to free-molecular. When $Kn > 10$, the gas is considered free-molecular and the vast majority of molecular interaction is with the structural surface and surface characteristics influence the flow. The Kn is used in experimental flow plots as the secondary axis to indicate the flow regime. Different model equations for each regime from Gallis and Torczynski (2012) are plotted in Fig. 9 along with experimental data. A single, closed-form model for all regimes, also from Gallis and Torczynski (2012), is plotted in Figures 10-13.

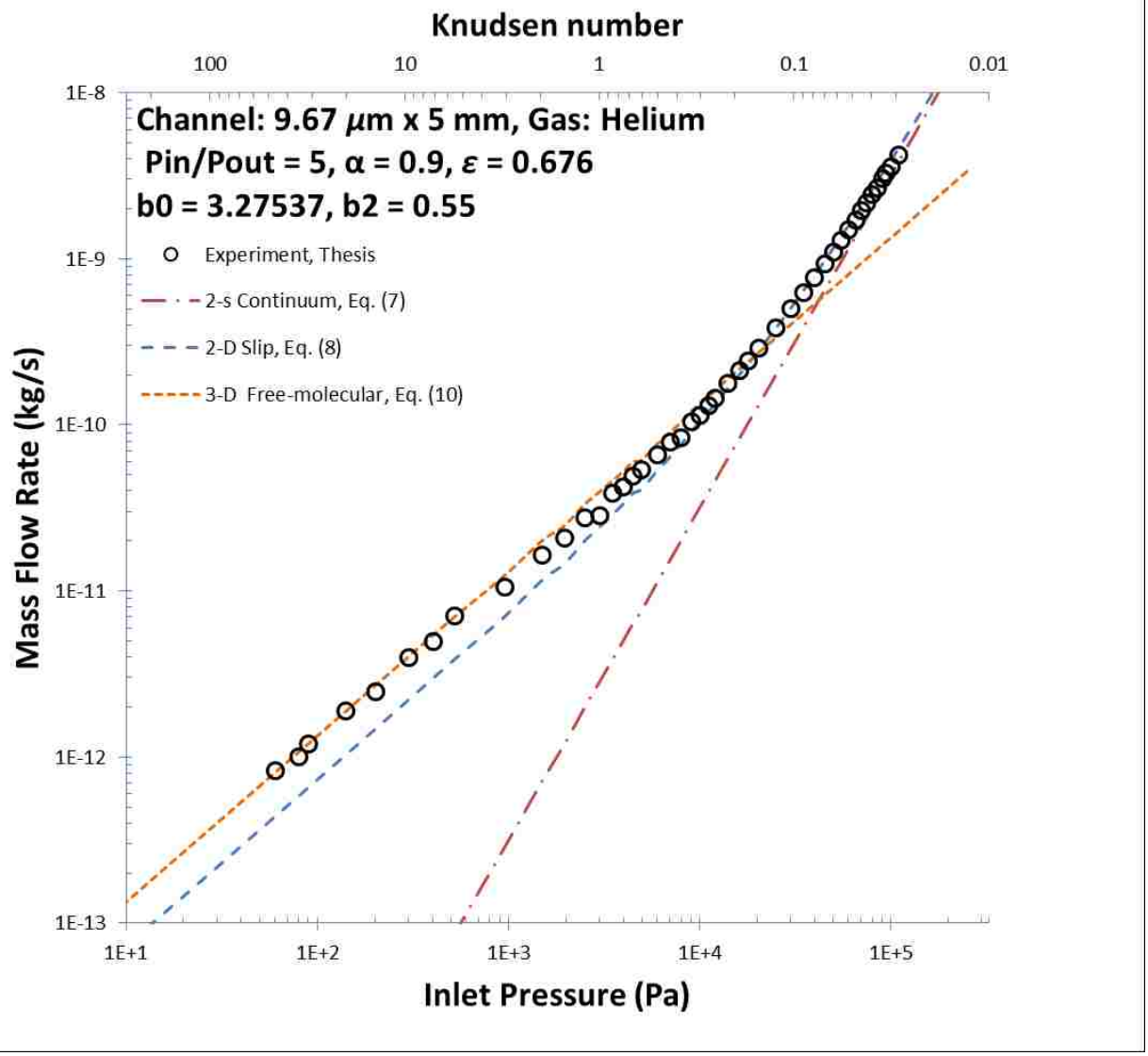

Figure 9 Experimental mass flow rates plotted against analytical expressions for the continuum, slip, and free-molecular regimes (Equation numbers refer to equations in the Theory section below.). The experimental data clearly transitions through the regimes as the driving pressure changes. At the far left, the experimental data follows the free-molecular prediction (orange dashed line) then transitions to the slip regime (blue dashed line) and finally up to the continuum regime (brown dashed line).

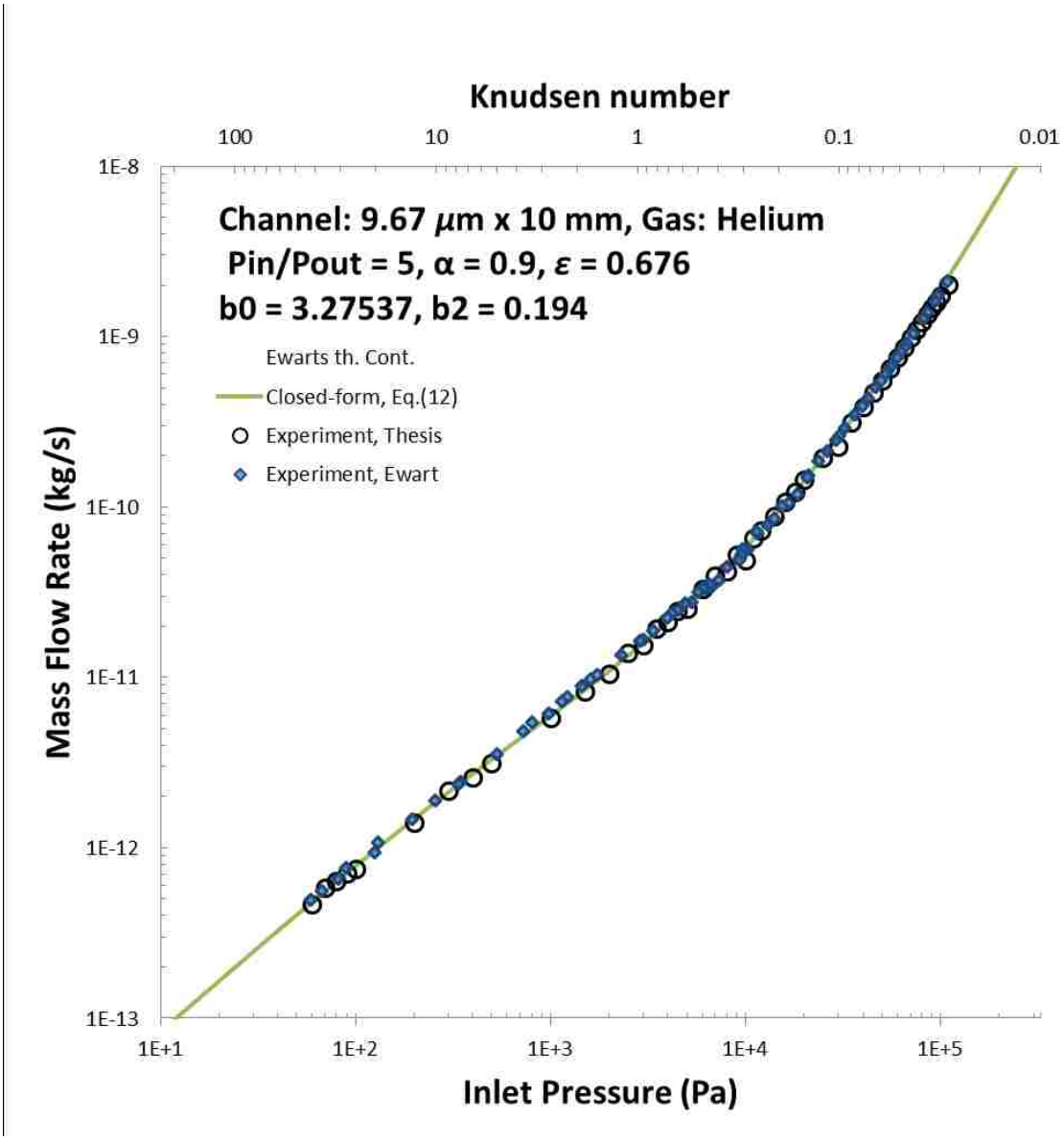

Figure 10 Experimental mass flow rate for a channel with 9.67 μm height and 10 mm length, plotted against DSMC based closed-form expression (Eq. 12) from Gallis and Torczynski (2012), also Eq 12 in the Theory section below. The details of the channel dimensions and experimental-based parameters are in the upper left corner. The Knudsen number is shown as the $\log_{10}$ upper horizontal axis.

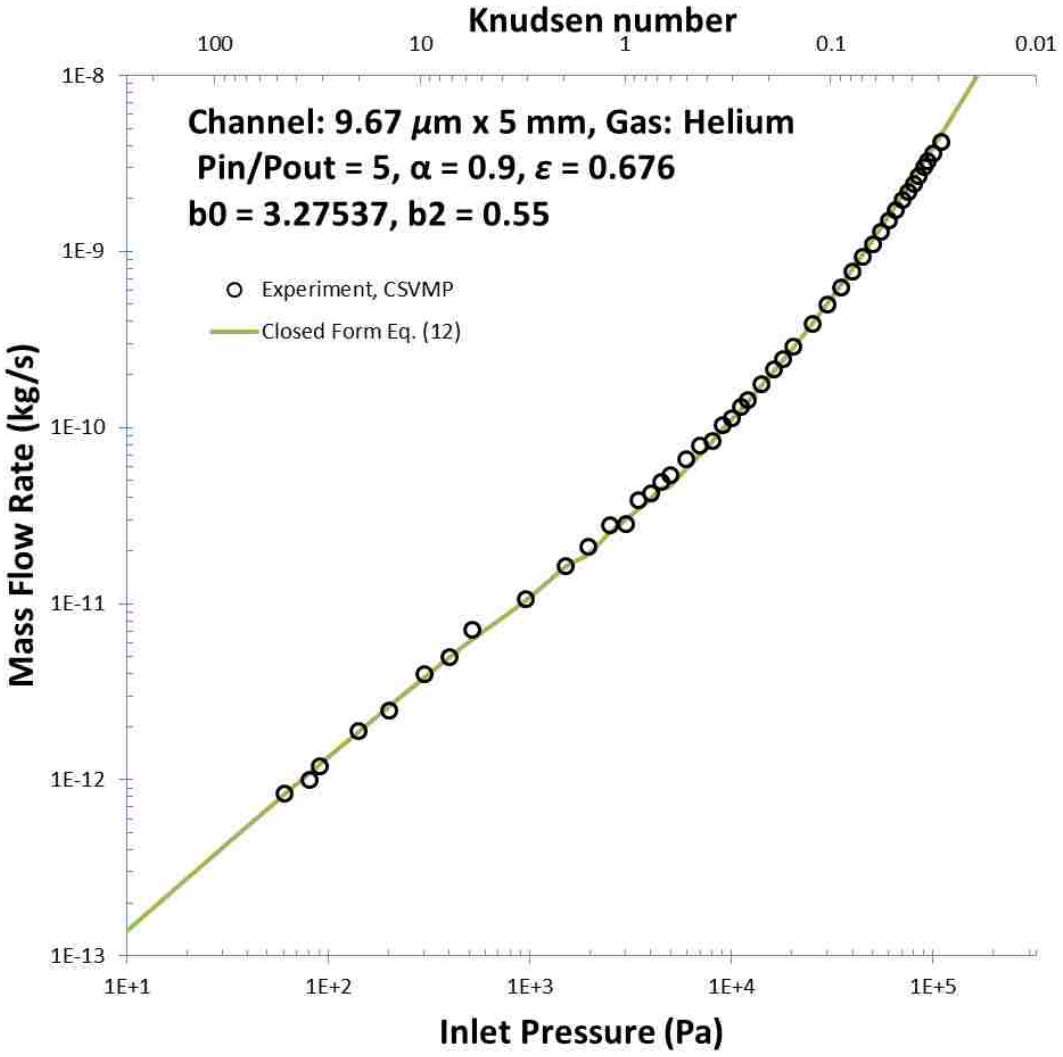

Figure 11 Experimental mass flow rate for a channel with 9.67 μm height and 5 mm length, plotted against DSMC based closed-form expression (Eq. 12) from Gallis and Torczynski (2012). The details of the channel dimensions and experimental-based parameters are in the upper left corner. The Knudsen number is shown as the $\log_{10}$ upper horizontal axis. The waviness at 1E+3 Pa is due to the inlet/outlet pressure ratio deviating from the standard 5:1. Since the pressures were manually set, they ranged from 6:1 and 4:1.

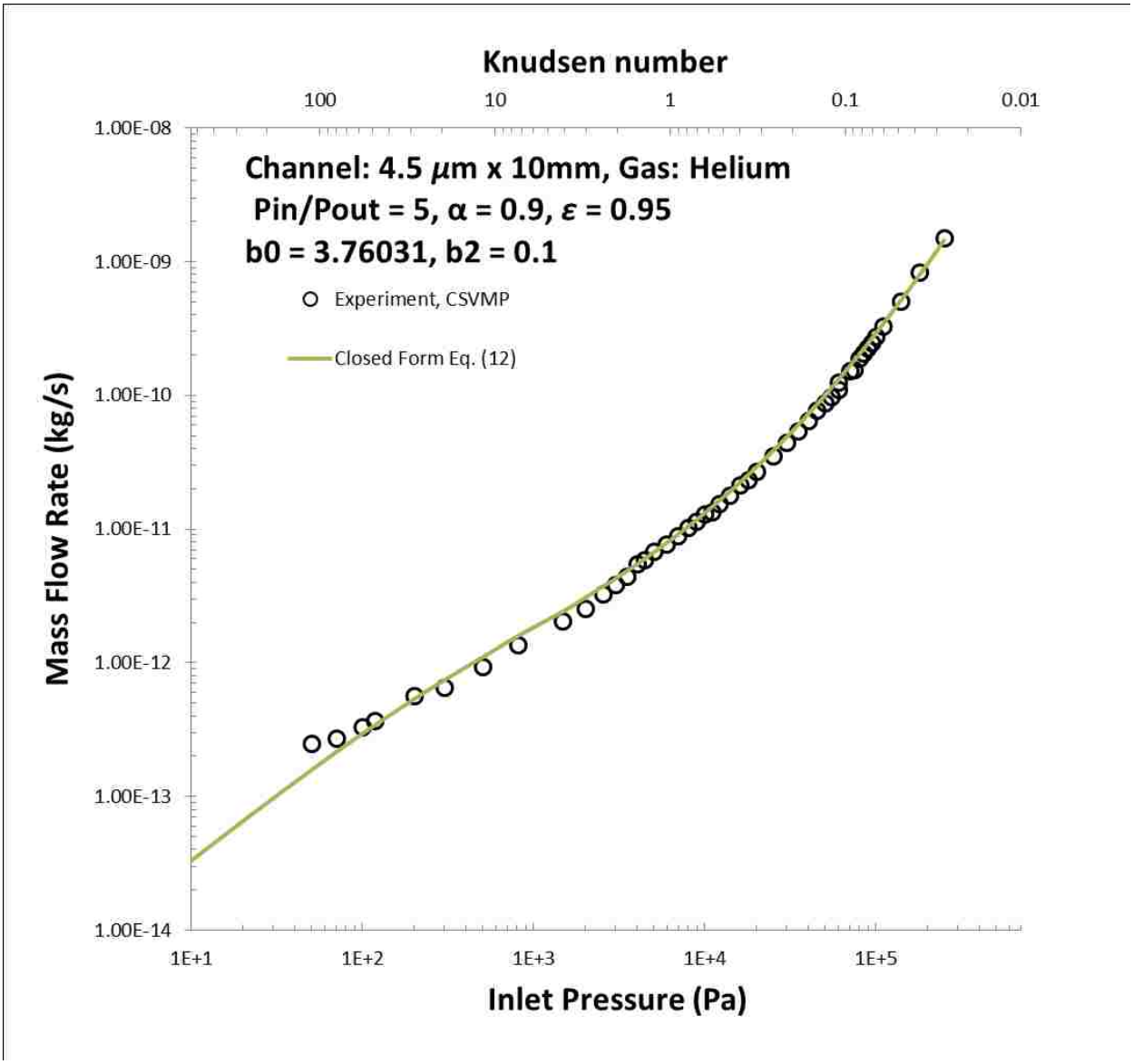

Figure 12 Experimental mass flow rate for a channel with 4.5 μm height and 10 mm length, plotted against DSMC based closed-form expression (Eq. 12) from Gallis and Torczynski (2012). The details of the channel dimensions and experimental-based parameters are in the upper left corner. The Knudsen number is shown as the $\log_{10}$ upper horizontal axis.

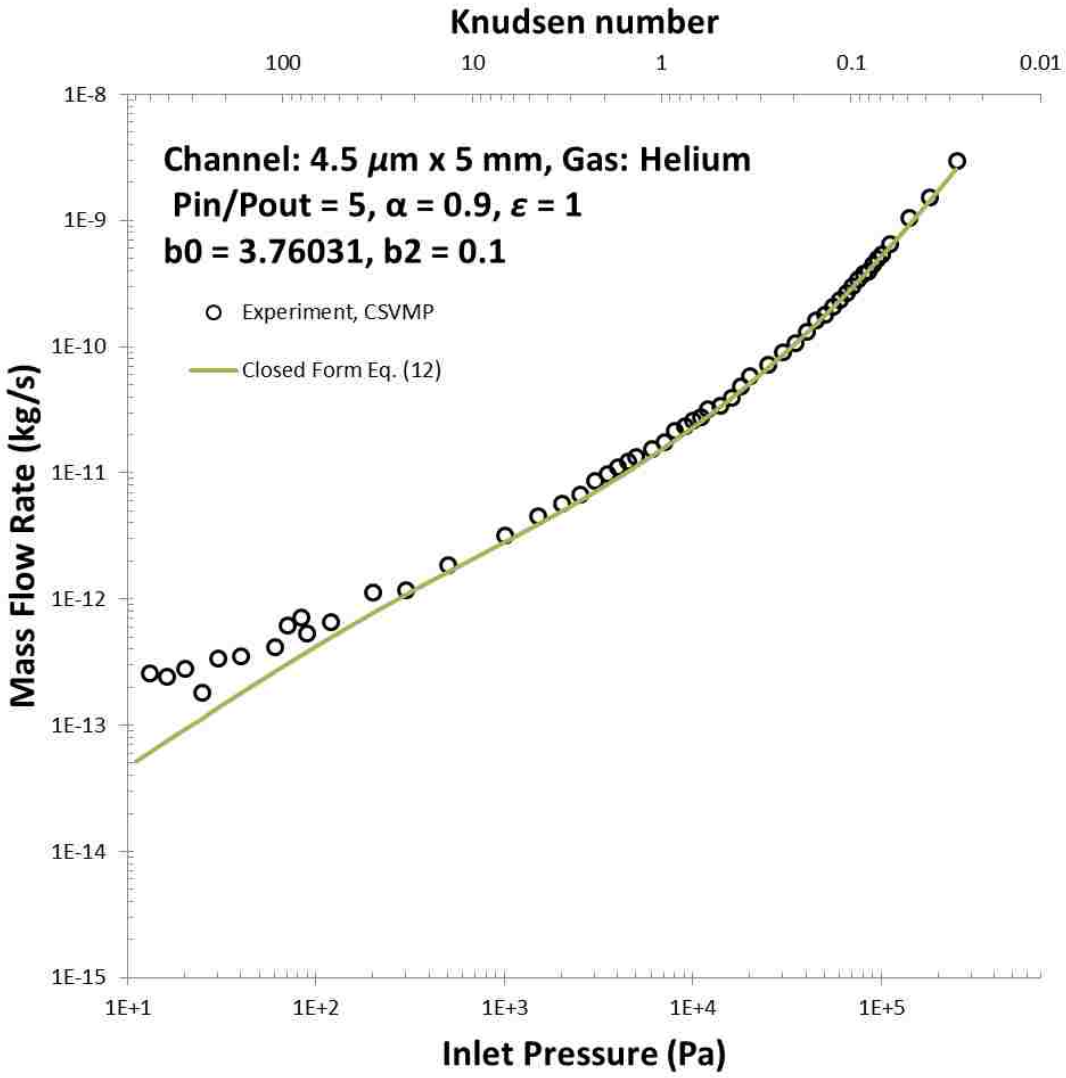

Figure 13 Experimental mass flow rate for a channel with 4.5 μm height and 5 mm length, plotted against DSMC based closed-form expression (Eq. 12) from Gallis and Torczynski (2012). The details of the channel dimensions and experimental-based parameters are in the upper left corner. The Knudsen number is shown as the $\log_{10}$ upper horizontal axis. The Knudsen number is a hefty 550 at the low end of this plot. Experimental data diverges from models by as much as 300% for the lowest measurements detailed in the discussion .

4.1 Theory

For reference, Fig. 1 shows a schematic diagram of the channel geometry. The rectangular channel has length *L*, width *W*, and height *H* (normal to the page). The channel wall is maintained at uniform temperature *T* and has a uniform tangential accommodation coefficient α, where $0 \leq \alpha \leq 1$. The channel joins two reservoirs of helium also at temperature *T*, with the inlet and outlet pressures p_1 and p_2 where p_1 / p_2 is approximately 5 for all of our experiments. Since $H/(\alpha L)$ is of the order of 10^{-3}, the effects of the inlet and outlet entry regions on the mass flow rate can be neglected.

As mentioned, the principal parameter of rarefied gas dynamics is the Knudsen number which characterizes the degree of rarefaction. Many different theoretical and numerical approaches have been used to analyze gas flow through a long channel under isothermal conditions. If the channel width *W* and length *L* are much larger than the channel height, one can neglect the end effects and lateral wall influence.

If the Knudsen number is very small ($Kn \ll 1$), the gas is considered a continuous medium and hydrodynamic equations can be applied to gas fow. Hence the name continuum or hydrodynamic regime. Experimental data in all regimes are evaluated against analytical closed-form expressions developed from Direct Simulation Monte Carlo (DSMC) models by Gallis and Torczynski (2012). The expressions were developed for steady isothermal flow through a microscale rectangular channel from continuum to free-molecular conditions for all values of the accommodation coefficient.

In the continuum regime, the mass flow rate can be calculated using the following analytical equation:

$$\dot{M}_c = \frac{2WH^3 p_m (p_1 - p_2)}{3\pi\mu c^2 L} \tag{7}$$

The subscript *c* denotes the continuum regime. The variable μ is the dynamic viscosity; the squared term *c* in the denominator is the mean thermal speed calculated by $c = (8k_bT/\pi m)^{0.5}$. Where k_b is Boltzmann's constant, *T* is temperature in Kelvin, and *m* is the molecular mass of helium is 6.65 x 10^{-24} grams. The pressure variables are easily calculated from measured data. The variable p_m is the mean pressure in the channel. *W*, *H*, and *L* are the channel width, height and length.

If the Knudsen number is larger, for reference, between 1 and 10, then the flow is not quite continuum, and not quite free-molecular. The intermediate regime is referred to as the slip regime signified by the subscript *s* and the analytical equation used solely for slip flow is:

$$\dot{M}_s = \dot{M}_c \left(1 + \frac{6p_\lambda}{p_m}\varpi_s\right), \tag{8}$$

where ϖ_s is the slip function:

$$\varpi_s = \frac{2-\alpha}{\alpha}(1 + b_1\alpha). \tag{9}$$

The term p_λ is the pressure at which the Knudsen number is unity. Experimental results in the near free molecular and free molecular regime denoted by the subscript *F* are plotted against:

$$\dot{M}_F = \dot{M}_c \left(\frac{6p_\lambda}{p_m}\varpi_F\right) \tag{10}$$

ϖ_F is the free-molecular function:

$$\varpi_F = \frac{2-\alpha}{\alpha}\varepsilon b_0\,. \tag{11}$$

The DSMC-based closed form equation developed by Gallis and Torczynski(2012) for isothermal steady flow through a rectangular channel at any Knudsen number is:

$$\dot{M} = \dot{M}_c \left(1 + \frac{6p_\lambda}{p_m} \varpi[p_1, p_2]\right) \quad (12)$$

Using the dimensionless function $\varpi[p_1, p_2]$ defined as:

$$\varpi[p_1, p_2] = \frac{2-\alpha}{\alpha}\left\{(1 + b_1\alpha) + \left(\varepsilon b_0 - (1 + b_1\alpha)\right)\frac{b_2 p_\lambda}{p_{1-}p_2} \ln\left[\frac{p_1 + b_2 p_\lambda}{p_2 + b_2 p_\lambda}\right]\right\} \quad (13)$$

As described in Gallis and Torczynski (2012),the parameter ε is based on experimental results, as is b_2 and α. Physically the limits for b_2 and α are set at , $0.1 < b_2 < 0.3$ and $0 < \alpha < 1$, 0 being full specular and 1 being full diffuse. The parameter ε is imperically determined and describes the channel end effects. ε =1 for and infinitely long channel. b_2 is also determined from experimental data and is used to match the data as the flow transitions from the slip to the free-molecular regime. The parameter $b_1$is 0.15 or very close for all common gases and all channels. The parameter b_0 gives the correct free-molecular limit and is a function of the channel width to height ratio. If *W/H*>1, then;

$$b_0 \approx 0.09682642 + 0.31831676 \ln\left[1 + 5.406189\frac{W}{H} + 8.018808\left(\frac{W}{H}\right)^2\right]. \quad (14)$$

b_0 is 3.27537 if the channel height is 9.67 μ m and 3.76031 if the channel height is 4.5 μ m.

4.2 Discussion

The experimental methods published by Ewart et al.(2007) provided an excellent starting point for our experiments. As noted for Fig. 10, our data matched quite well compared to Ewart's for a channel of similar dimensions. This was the first step in verifying that our measurement system was sufficient to implement the 'constant volume' technique. We were then able to compare our data for four different channel dimensions to models by Galis and Torczynski(2012) which also matched quite well with the exception of the

lowest few data points of our measurements. The experimental data started to deviate from the model when the mean Kn was approximately 30 and greater. When Kn is 30, the mean free path (λ) was 135 μm. Our lowest measurement, also the furthest from model, was where the mean Kn was 550 and the MFP was 2.5 mm, five times larger than the channel width. The model assumes $W >> \lambda$ and does not account for sidewall interaction. As Kn approaches 30 in our experiments, this assumption does not hold and may be partially to blame for the deviation.

Another factor that may contribute to this discrepancy is that the outlet pressure for these measurements was very close to 10 Pa, pushing the limits of the Paroscientific Model 745 gage. Although the Paroscientific gage is a primary laboratory standard, it is intended for higher pressures and is only calibrated down to 10 kPa. That is not to say the gage is not accurate lower than 10 kPa, but it must be characterized with a calibrated gage. In fact, benchmarking against Ewart's data illustrates that the gage performs well for pressures much lower than the 10 kPa stated limit. For future work, the Paroscientific 745 will be characterized with calibrated Baratron pressure transducers as well as a Spinning Rotor Gage (SRG), which is well suited to the low pressure regimes covered in this thesis.

Secondly, the system may be experiencing some outgassing during prolonged periods of vacuum which pertain at high Kn regime of measurements. Stray molecules from the system may very easily make their way into the flowing gas, giving an undesired increase in flow.

The length-to-width ratio of the 4.5 μm X 5 mm channel used for the lowest flow measurements stretches the model assumptions. One of the main assumptions used in the

models is that $L>>W$ and for this case, L is only larger than W by a factor of 10 for this channel. Channeling of the flowing molecules may be occurring in the shorter channel and molecules may be able to shoot across the entire length of the channel before colliding with any of the channel surfaces. In the future, experiments at the same pressures for the 10 mm long channel of the same height would provide some verification of this hypothesis.

5 Conclusion

Gas flow measurements through rectangular cross-section microchannels are investigated. The gas is helium and the flow is isothermal and steady for each measurement. The intention is to measure flows for a wide Knudsen range, specifically focusing on the high Knudsen range. The calculated Kn mean for our experimental conditions ranged from 0.01 to 550, well into the free-molecular regime. Flow was able to reach the free-molecular regime thanks to micro-dimensioned channels and a precise measurement system. Flows on the order of 10^{-13} kgs^{-1} were measured. To put this into perspective, it would take approximately 300,000 years to accumulate 1kg of helium. The measured mass flow rates agree with the model equations from Gallis and Torzcynski (2012) until the Knudsen number increases above 100 for the 4.5 μm x 5 mm channel. Then, only deviation occurs where experimental values are higher than those predicted by theory. This may be attributed to the smaller L/W ratio, so end effects may be contributing to some of the flow. This data is valuable and provides a step towards the next stage in fully understanding rarefied gas dynamics.

References:

Arkilic, E. B., M. A. Schmidt, et al. (1997). "Gaseous slip flow in long microchannels." Journal of Microelectromechanical Systems **6**(2): 167-178.

Ewart, T., P. Perrier, et al. (2007). "Tangential momemtum accommodation in microtube." Microfluidics and Nanofluidics **3**(6): 689-695.

Ewart, T., P. Perrier, et al. (2007). "Mass flow rate measurements in a microchannel, from hydrodynamic to near free molecular regimes." Journal of Fluid Mechanics **584**: 337.

Farrens, S. N., J. R. Dekker, et al. (1995). "CHEMICAL FREE ROOM-TEMPERATURE WAFER TO WAFER DIRECT BONDING." Journal of the Electrochemical Society **142**(11): 3949-3955.

Fissell, W. H., A. T. Conlisk, et al. (2011). "High Knudsen number fluid flow at near-standard temperature and pressure conditions using precision nanochannels." Microfluidics and Nanofluidics **10**(2): 425-433.

Gallis, M. A. and J. R. Torczynski (2012). "Direct simulation Monte Carlo-based expressions for the gas mass flow rate and pressure profile in a microscale tube." Physics of Fluids **24**(1).

Graur, I. A., J. G. Méolans, et al. (2005). "Analytical and numerical description for isothermal gas flows in microchannels." Microfluidics and Nanofluidics **2**(1): 64-77.

Howlader, M. M. R., S. Suehara, et al. (2006). "Room-temperature microfluidics packaging using sequential plasma activation process." Ieee Transactions on Advanced Packaging **29**(3): 448-456.

Howlader, M. R. (2010). MEMS/Microfluidics Packaging Without Heating. Reliability, Packaging, Testing, and Characterization of Mems/Moems and Nanodevices Ix. R. C. R. R. Kullberg. **7592**.

Lin, X. H., Z. W. Ma, et al. (2006). Impacts of wafer-bow and surface contamination on low temperature wafer direct bonding.

Marino, L. (2009). "Experiments on rarefied gas flows through tubes." Microfluidics and Nanofluidics **6**(1): 109-119.

Pitakarnnop, J., S. Varoutis, et al. (2009). "A novel experimental setup for gas microflows." Microfluidics and Nanofluidics **8**(1): 57-72.

Porodnov, B. T., P. E. Suetin, et al. (1974). "EXPERIMENTAL INVESTIGATION OF RAREFIED-GAS FLOW IN DIFFERENT CHANNELS." Journal of Fluid Mechanics **64**(JUL8): 417-437.

Schmidt, M. A. (1994). "Silicon wafer bonding for micromechanical devices." Technical Digest. Solid-State Sensor and Actuator Workshop.

Sharipov, F. (1999). "Rarefied gas flow through a long rectangular channel." Journal of Vacuum Science & Technology a-Vacuum Surfaces and Films **17**(5): 3062-3066.

Szalmas, L., J. Pitakarnnop, et al. (2010). "Comparative study between computational and experimental results for binary rarefied gas flows through long microchannels." Microfluidics and Nanofluidics **9**(6): 1103-1114.

Tang, Z. R., P. Peng, et al. (2009). "Effect of nanoscale surface topography on low temperature direct wafer bonding process with UV activation." Sensors and Actuators a-Physical **151**(1): 81-86.

APPENDICES

APPENDIX A: Experimental Data for Channel: L = 10mm, H = 9.67 μm, W = 500 μm

P in (Pa)	P out (Pa)	Measured Mass Flow Rate (kg/s)
110482	22096	2.03E-09
99876	19975	1.74E-09
94930	18986	1.6E-09
90388	18077	1.47E-09
85144	17028	1.35E-09
79162	15832	1.22E-09
75469	15093	1.1E-09
69996	13999	9.82E-10
64578	12915	8.63E-10
60231	12046	7.56E-10
55312	11062	6.5E-10
49997	9999	5.56E-10
46014	9202	4.69E-10
40842	8168	3.87E-10
35279	7055	3.14E-10
29910	5982	2.26E-10
24896	4979	1.94E-10
20378	4075	1.45E-10
18054	3610	1.23E-10
15989	3197	1.07E-10
14050	2810	8.89E-11
12108	2421	7.24E-11
10977	2195	6.56E-11

P in (Pa)	P out (Pa)	Measured Mass Flow Rate (kg/s)
10030	2006	4.84E-11
8992	1798	5.22E-11
8010	1602	4.21E-11
7021	1404	3.97E-11
5989	1197	3.33E-11
5015	1003	2.52E-11
4567	913.4	2.45E-11
4018	803.6	2.12E-11
3506	701.2	1.94E-11
2992	598.4	1.55E-11
2517	503.4	1.4E-11
1993	398.6	1.05E-11
1515	303.0	8.25E-12
998.1	199.6	5.75E-12
502.3	100.4	3.17E-12
399.8	79.96	2.58E-12
299.8	59.96	2.16E-12
202.4	40.48	1.40E-12
100.5	20.10	7.50E-13
90.62	18.12	7.10E-13
80.34	16.06	6.40E-13
69.87	13.97	5.85E-13
61.03	12.21	4.67E-13

APPENDIX B: Experimental Data for Channel: L = 5mm, H = 9.67 μm, W = 500 μm

P in (Pa)	P out (Pa)	Measured Mass Flow Rate (kg/s)
109191	22252	2.03E-09
99738	20252	1.74E-09
94259	18798	1.6E-09
90393	17865	1.47E-09
84526	17065	1.35E-09
79860	16119	1.22E-09
74794	14932	1.1E-09
70128	13999	9.82E-10
65061	13079	8.63E-10
59995	12119	7.56E-10
54929	11026	6.5E-10
49929	10013	5.56E-10
44903	8986	4.69E-10
39783	8013	3.87E-10
34784	6986	3.14E-10
29878	5933	2.26E-10
25051	5036	1.94E-10
20318	4080	1.45E-10
17972	3614	1.23E-10
16145	3198	1.07E-10
13967	2726	8.89E-11
11960	2450	7.24E-11
11090	2241	6.56E-11

P in (Pa)	P out (Pa)	Measured Mass Flow Rate (kg/s)
9971	2052	4.84E-11
8982	1821	5.22E-11
7983	1807	4.21E-11
6973	1629	3.97E-11
5974	1425	3.33E-11
4962	1291	2.52E-11
4482	913.3	2.45E-11
3953	854.6	2.12E-11
3468	741.3	1.94E-11
2985	633.3	1.55E-11
2486	518.6	1.4E-11
1952	485.3	1.05E-11
1499	301.3	8.25E-12
947.9	214.6	5.75E-12
517.3	103.9	3.17E-12
399.8	79.96	2.58E-12
299.8	59.96	2.16E-12
202.4	40.48	1.40E-12
138.5	28.13	7.50E-13
90.62	18.12	7.10E-13
80.34	16.07	6.40E-13
69.87	13.97	5.85E-13
61.03	12.21	4.67E-13

APPENDIX C: Experimental Data for Channel: L = 10mm, H = 4.5 μm, W = 500 μm

P in (Pa)	P out (Pa)	Measured Mass Flow Rate (kg/s)
249866	48971	1.5E-09
180240	36048	8.3E-10
139981	27898	5.1E-10
109458	21998	3.2884E-10
99538	20076	2.7769E-10
94499	18998	2.4763E-10
89686	18079	2.2712E-10
84460	17052	2.0766E-10
79713	16079	1.8817E-10
74647	15052	1.5646E-10
69954	14052	1.5292E-10
60075	11986	1.263E-10
59888	12131	1.1144E-10
54889	11042	9.7916E-11
49976	10050	8.7664E-11
45044	9043	7.7263E-11
40014	8038	6.5376E-11
34909	7026	5.4381E-11
30064	6022	4.4426E-11
24938	5010	3.5214E-11
19954	4033	2.6893E-11
17877	3609	2.3625E-11
16024	3216	2.1247E-11
13863	2808	1.783E-11

P in (Pa)	P out (Pa)	Measured Mass Flow Rate (kg/s)
12071	2409	1.545E-11
10987	2208	1.337E-11
10015	2007	1.308E-11
8931	1808	1.144E-11
7987	1603	1.025E-11
6930	1403	8.915E-12
5977	1206	7.726E-12
5031	1004	6.835E-12
4453	902.7	5.892E-12
3999	805.1	5.498E-12
3489	698.7	4.417E-12
2988	603.4	3.82E-12
2521	498.0	3.286E-12
2006	401.6	2.572E-12
1478	303.8	2.047E-12
812.7	153.7	1.357E-12
505.6	98.53	9.4E-13
307.3	59.64	6.5E-13
209.9	41.33	5.71E-13
117.3	23.46	3.71E-13
102.5	19.34	3.31E-13
70.45	13.76	2.71E-13
48.91	8.98	2.51E-13

APPENDIX D: Experimental Data for Channel: L = 5mm, H = 4.5 μm, W = 500 μm

P in (Pa)	P out (Pa)	Measured Mass Flow Rate (kg/s)
251023	50205	3.010E-09
179942	35988	1.550E-09
140321	28064	1.049E-09
111020	22204	6.610E-10
98698	19740	5.380E-10
94499	18998	4.950E-10
89686	18079	4.501E-10
84460	17052	3.993E-10
79713	16079	3.861E-10
74647	15052	3.469E-10
69954	14052	3.073E-10
60075	11986	2.674E-10
59888	12131	2.379E-10
54889	11042	2.080E-10
49976	10050	1.825E-10
45044	9043	1.634E-10
40014	8038	1.321E-10
34909	7026	1.085E-10
30064	6022	9.153E-11
24938	5010	7.281E-11
19954	4033	5.943E-11
17877	3609	4.874E-11
16024	3216	4.012E-11
13863	2808	3.417E-11
12071	2364	3.209E-11
10987	2208	2.764E-11
10015	2007	2.630E-11

P in (Pa)	P out (Pa)	Measured Mass Flow Rate (kg/s)
8931	1808	2.362E-11
7987	1603	2.154E-11
6930	1403	1.753E-11
5977	1206	1.560E-11
5031	1004	1.352E-11
4453	902.7	1.248E-11
3999	805.1	1.129E-11
3489	698.7	9.955E-12
2988	603.4	8.766E-12
2521	498.0	6.835E-12
2006	401.6	5.795E-12
1478	303.8	4.606E-12
978.5	186.9	3.215E-12
488.3	104.40	1.880E-12
302.2	62.33	1.189E-12
198.2	38.94	1.141E-12
119.99	23.89	6.603E-13
88.52	17.71	5.349E-13
82.66	16.53	7.132E-13
71.41	14.47	6.240E-13
58.69	11.87	4.160E-13
39.65	8.134	3.566E-13
29.77	6.072	3.377E-13
24.67	5.200	1.813E-13
20.13	4.026	2.823E-13
16.13	3.226	2.422E-13
13.13	2.626	2.594E-13

APPENDIX E: Wafer Bow Measurements

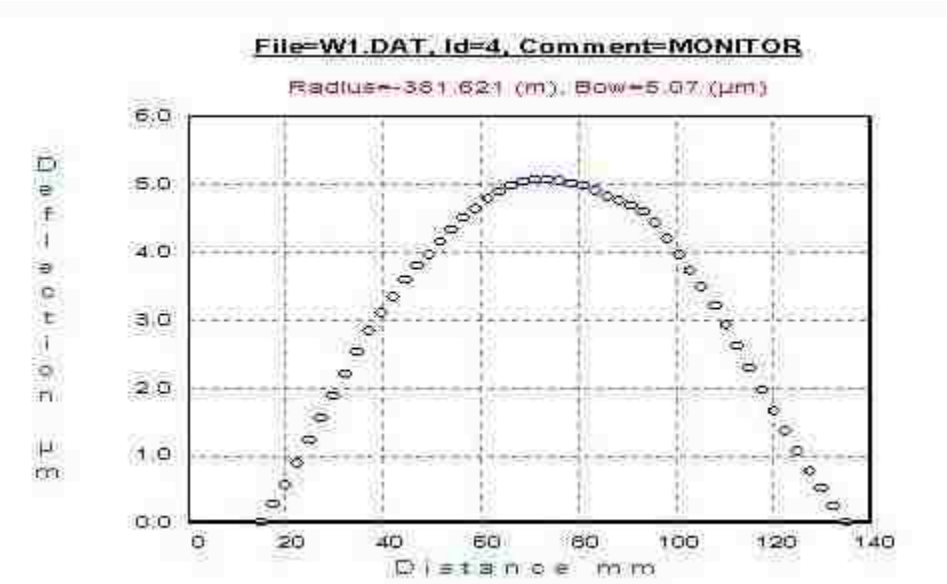

CONTROL: This is a 670 *n*m laser scan of a single crystal monitor wafer for reference. Notice a "stress-free" wafer still has ~5 μm of bow which is negligible over the 150 mm diameter. The following images are scans of SOI wafers before and after the backside oxide was grown. Above each image is the measured radius of curvature in meters called "radius" and the measured bow across the wafer in micrometers called "bow".

150mm SOI wafer with 4 μm device bow measurement

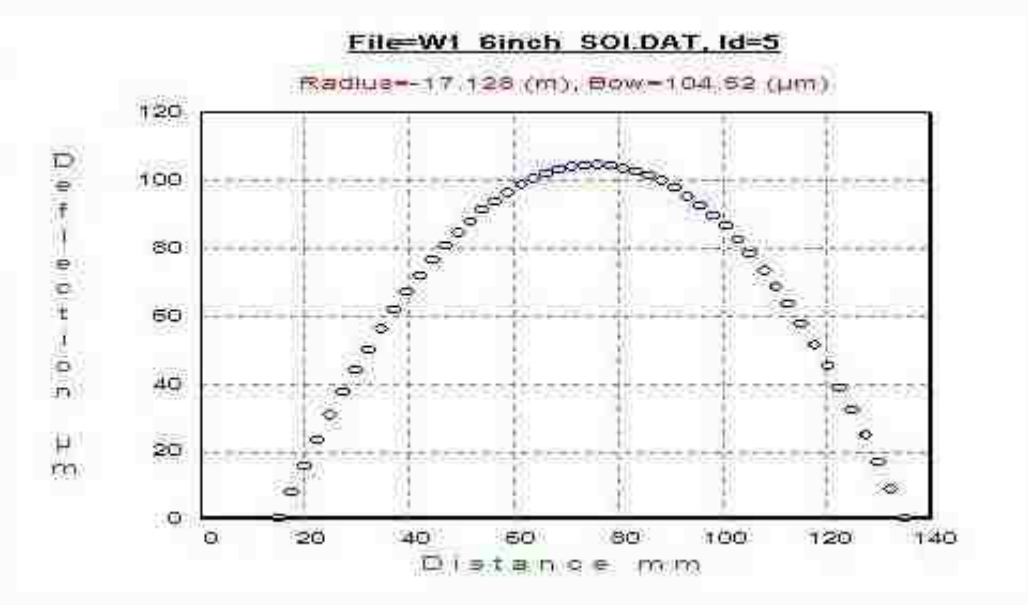

W1 4/1/400 SOI before oxide

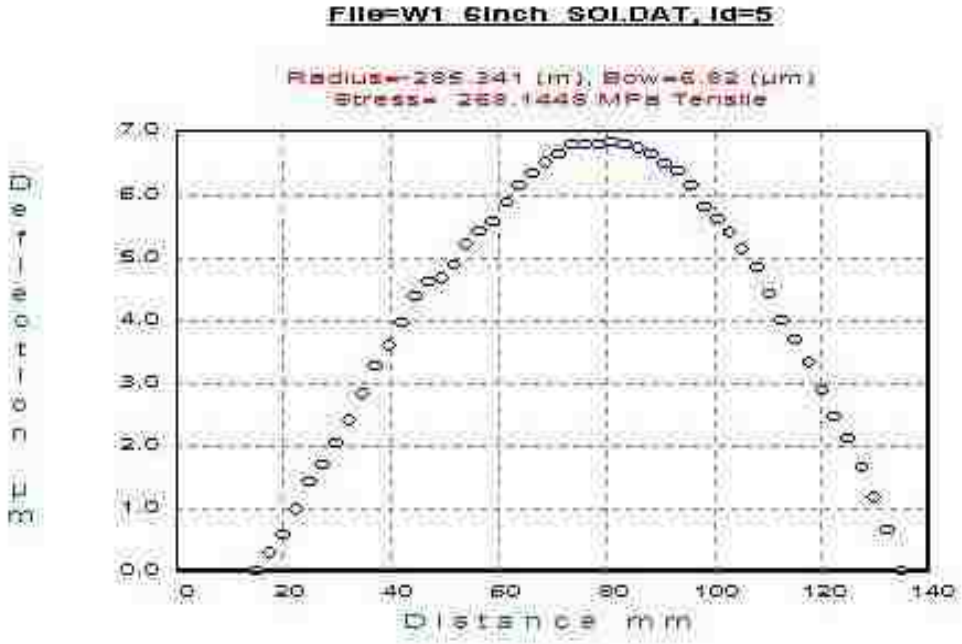

W1 4/1/400 SOI after oxide: notice the radius of curvature increased from 17 m to 285 m and the bow decreased from 104.5 μm to 6.82 μm.

SOI wafer with 9 μm device bow measurement

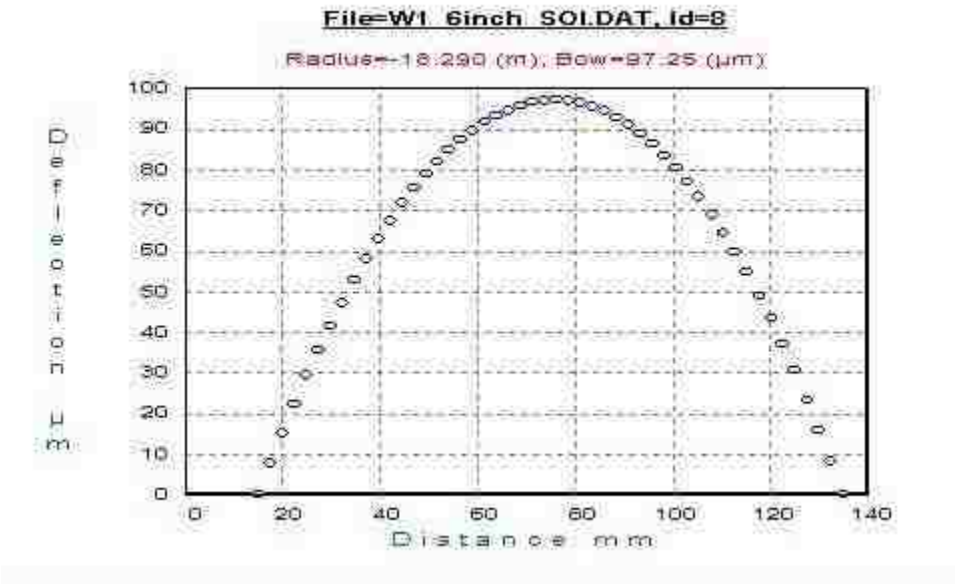

W2 9/1/400 SOI before oxide

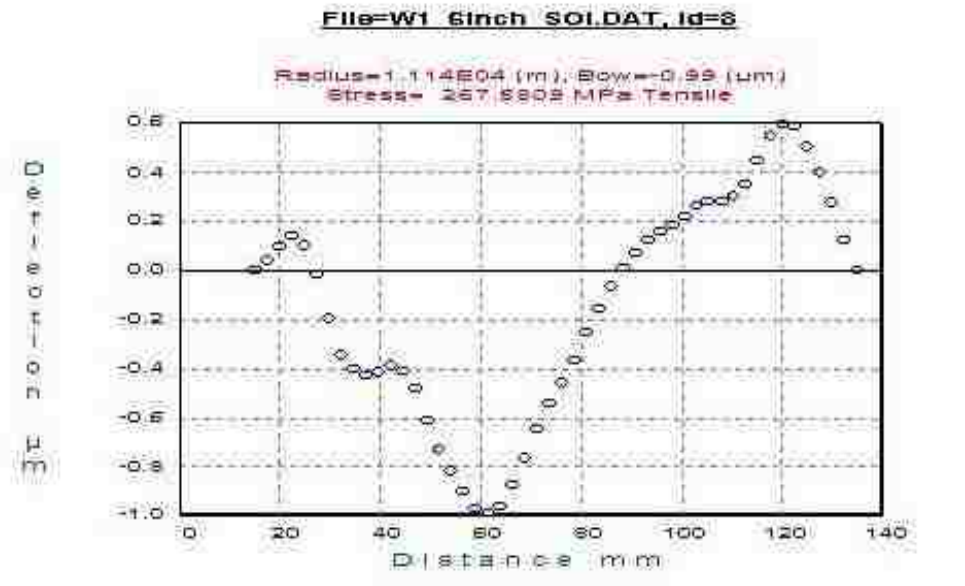

W1 4/1/400 SOI after oxide: notice the radius of curvature increased from 18 m to over 1000 m and the bow decreased from 104.5 μm to less than 1 μm. This particular wafer had the best results from the bow removal.

APPENDIX F: C-Mode Scanning Acoustic Microscopy (CSAM) Images

For the following, the dark areas are bonded and the light areas are voids.

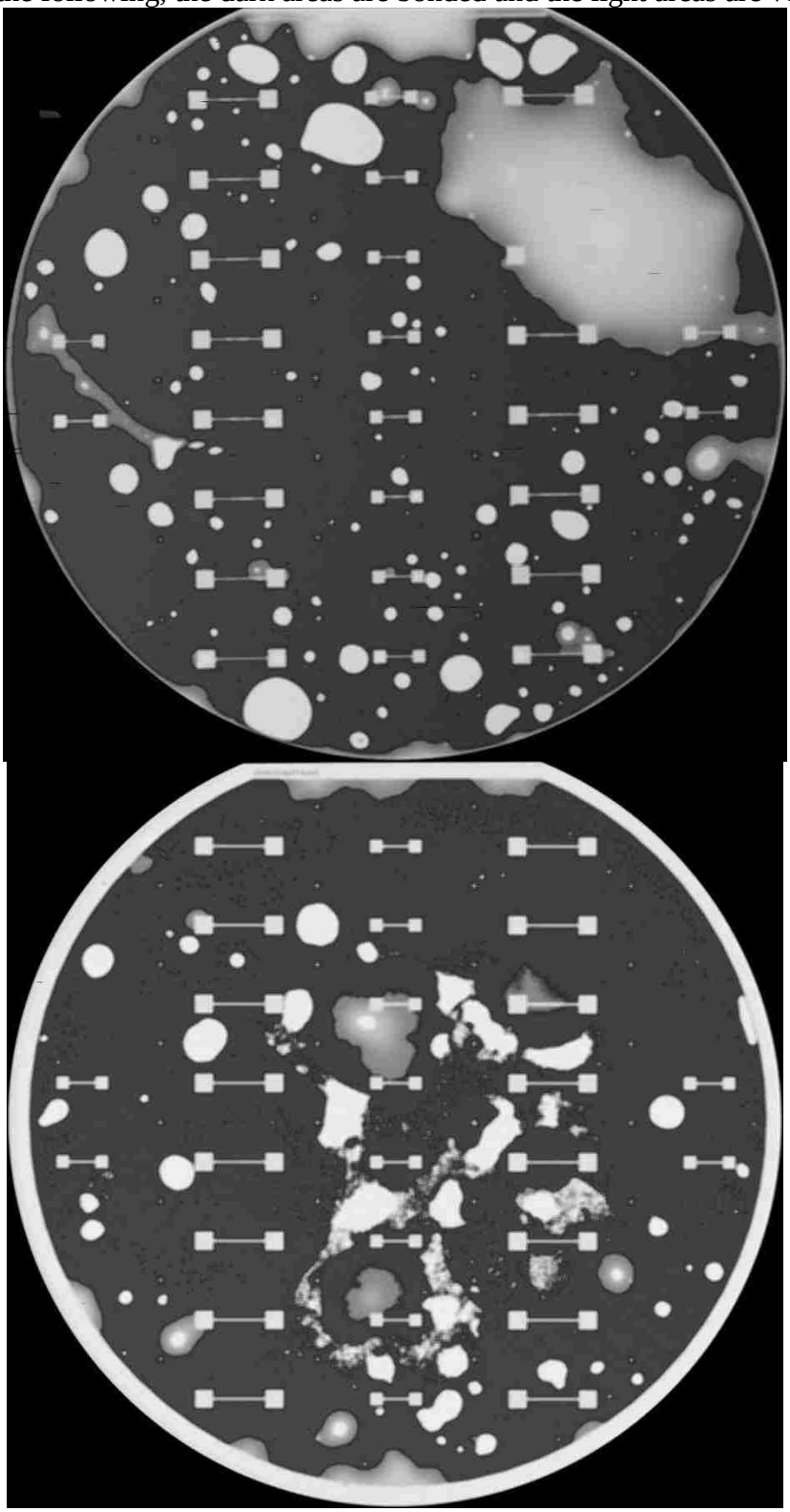

For the following, the light areas are bonded and the dark areas are voids.

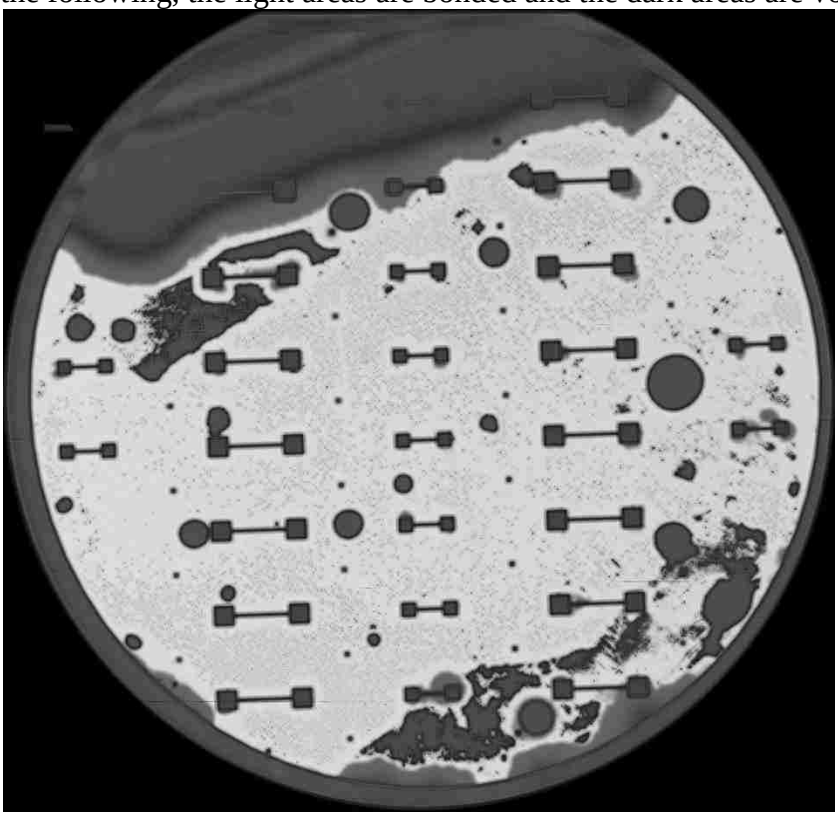

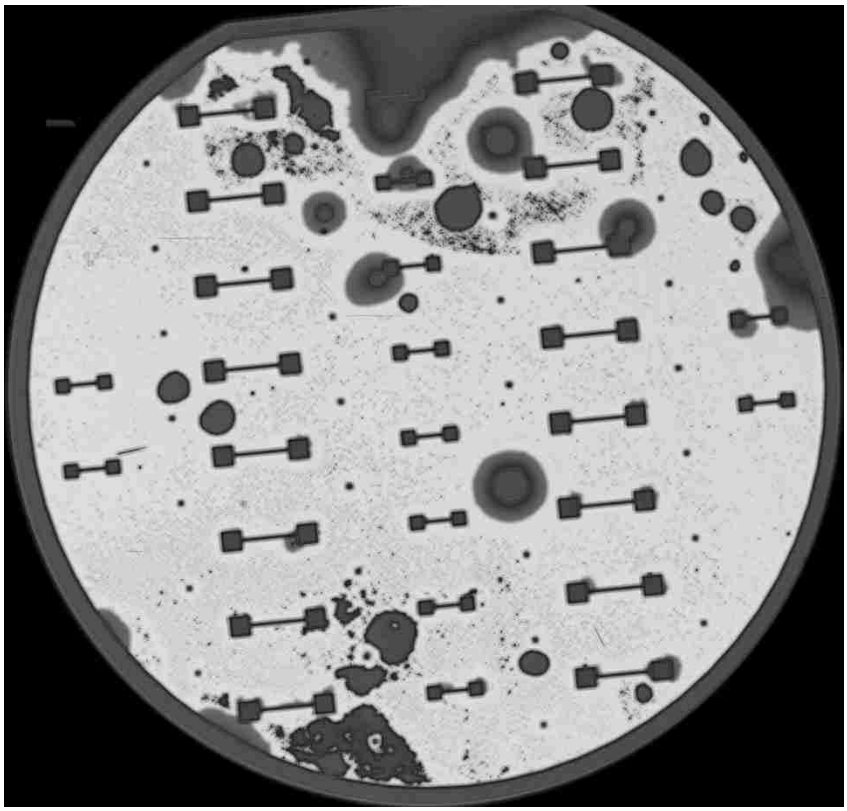

This figure depicts a poorly bonded wafer which is an example of an attempted bond before the backside oxide to remove wafer bow and edge bead removal.

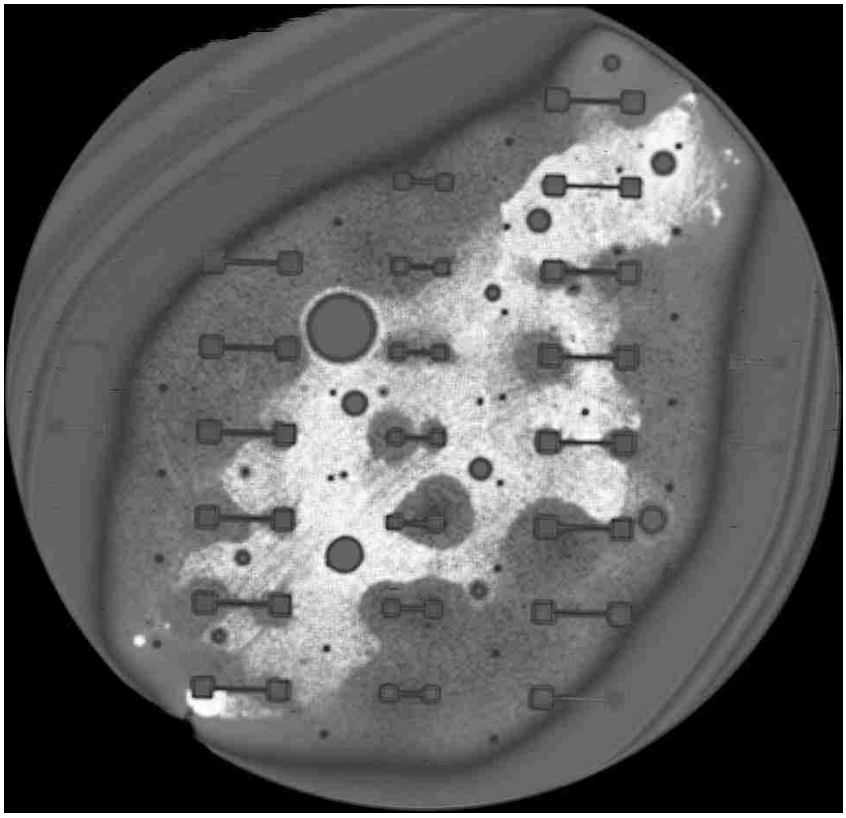

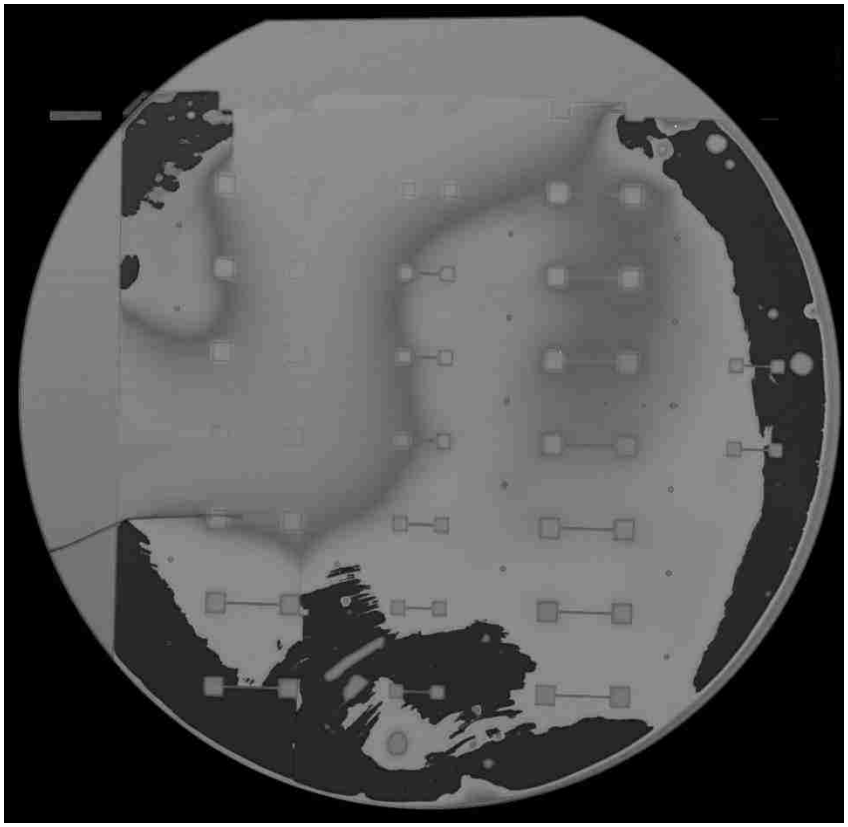

APPENDIX G: Edge Bead removal scans

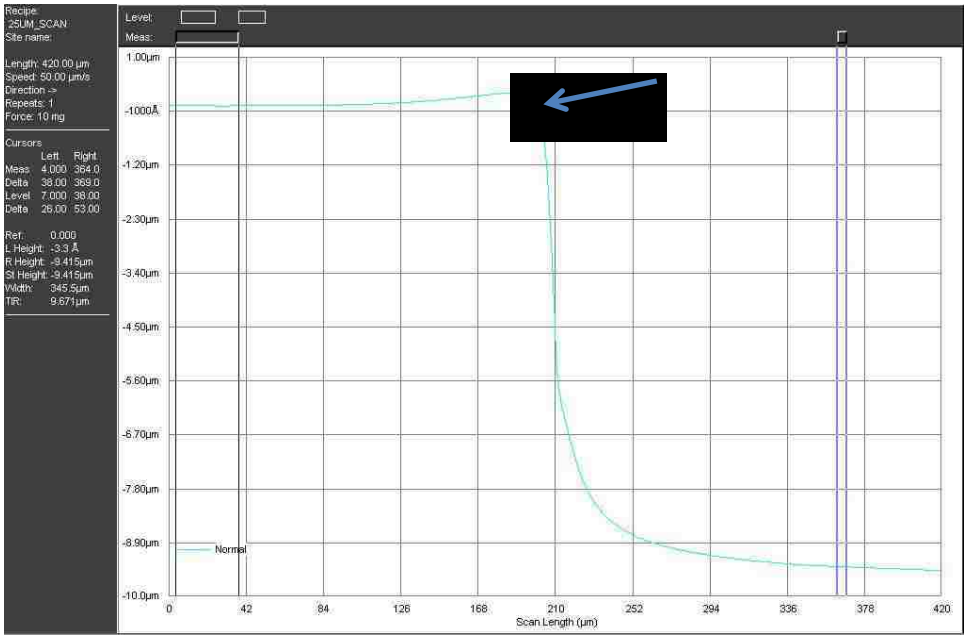

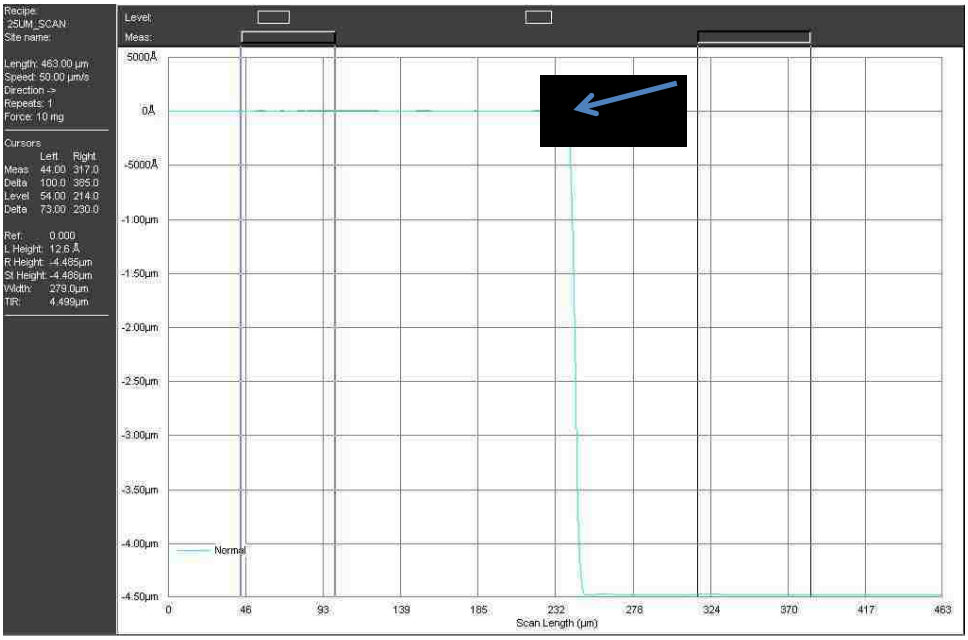

A small 0.25 μm lip around the edge of the wafer existed from the manufacturer. It is believed that this lip is a result of the SOI manufacturing process as two wafers are bonded together and one is thinned using chemical mechanical polishing to achieve the desired device layer thickness.